Advanced Energy Materials

ADVANCED ENERGY MATERIALS
www.advenergymat.de

RESEARCH ARTICLE

High-Performance Elastomeric Lithium Metal Anodes Enabled by a Lithiophilic Monolayer-Assembled Nano-Crumpled Micro-Concave Architecture

Sungha Choi[1] | Donghyeon Nam[2] | Geon Choi[3] | Seonho Lee[1] | Seungeun Paik[4] | Yongkwon Song[5] | Seungyeop Choi[6] | Jaejin Lim[6] | Woojae Chang[1] | Jeong Gon Son[3,7] | Daegun Kim[8] | Giwon Lee[9] | Sungjun Park[10,11] | Yong Min Lee[6] | Seoin Back[3,12] | Yongmin Ko[13] | Jinhan Cho[1,3,7]

[1]Department of Chemical and Biological Engineering, Korea University, Seoul, Republic of Korea | [2]The George W. Woodruff School of Mechanical Engineering, Georgia Institute of Technology, Atlanta, Georgia, USA | [3]KU-KIST Graduate School of Converging Science & Technology, Korea University, Seoul, Republic of Korea | [4]Department of Mechanical Engineering, Seoul National University, Seoul, Republic of Korea | [5]Department of Materials Science and Engineering, Northwesthern University, Evanston, Illinois, USA | [6]Department of Chemical and Biomolecular Engineering, Yonsei University, Seoul, Republic of Korea | [7]Soft Hybrid Materials Research Center, Korea Institute of Science and Technology (KIST), Seoul, Republic of Korea | [8]School of Chemical, Biological and Battery Engineering, Gacheon University, Seongnam, Republic of Korea | [9]Department of Chemical Engineering, Kwangwoon University, Seoul, Republic of Korea | [10]Department of Intelligence Semiconductor Engineering, Ajou University, Suwon, Republic of Korea | [11]Department of Electrical and Computer Engineering, Ajou University, Suwon, Republic of Korea | [12]Institute for Multiscale Matter and Systems (IMMS), Ewha Womans University, Seoul, Republic of Korea | [13]Division of Energy & Environmental Technology, Materials Research Institute, Daegu Gyeongbuk Institute of Science and Technology (DGIST), Daegu, Republic of Korea

Correspondence: Seoin Back (sback@korea.ac.kr) | Yongmin Ko (yongmin.ko@dgist.ac.kr) | Jinhan Cho (jinhan71@korea.ac.kr)

Received: 25 February 2026 | **Revised:** 30 April 2026 | **Accepted:** 13 May 2026

Keywords: elastomeric lithium metal anode | Li dendritic growth | lithium metal batteries | renewable energy

ABSTRACT

Li metal batteries are promising next-generation energy storage systems due to their high theoretical energy density and low redox potential. However, their practical application is limited by Li dendrite formation during repeated cycling, which compromises safety and shortens cycle life. Herein, we introduce a flexible elastomeric Li metal anode that integrates a lithiophilic monolayer-assembled nano-crumpled surface with microscale concave architectures. This hierarchical design was realized by densely assembling metal nanoparticles onto thiol-functionalized elastomer, followed by Ni electroplating and subsequent assembly with lithiophilic amine-terminated molecular linkers. The resulting elastomeric anode effectively reduced Li nucleation overpotential and promotes mossy Li deposition. As a result, symmetric cells exhibited excellent cycling stability for over 2,100 h at 3 mA cm^{-2}/3 mAh cm^{-2}. Moreover, Li||$LiFePO_4$ full cells retained ~90.2% capacity after 1,000 cycles at 1C, demonstrating the potential of chemically and structurally engineered elastomeric anodes for durable and safe Li metal batteries.

1 | Introduction

The rising demand for energy storage devices with high energy density is crucial for applications such as electric vehicles and flexible or portable electronics. This need has spurred intensive research into next-generation lithium-ion batteries (LIBs) that exceed the performance of those currently available commercially. Lithium (Li) metal is particularly notable among various

Sungha Choi, Donghyeon Nam, and Geon Choi contributed equally to this work.

high-energy materials, owing to its exceptionally high theoretical specific capacity of 3,861 mAh g^{-1}, minimal electrochemical potential of −3.04 V relative to the standard hydrogen electrode (SHE), and low mass density of 0.534 g cm^{-3}. Consequently, Li metal batteries (LMBs) are noted for their significant theoretical energy densities, making them highly attractive for advanced energy storage technologies [1–3]. However, their practical application is hindered by significant challenges, such as the uncontrollable growth of Li dendrites during repetitive charging and discharging cycles [1, 4]. This dendritic growth mechanically ruptures and destabilizes the solid-electrolyte-interphase (SEI) layer [5, 6], thereby decreasing Coulombic efficiency, accelerating capacity degradation, and severely undermining the operational stability of batteries, presenting serious safety concerns.

Extensive efforts have been devoted to mitigating Li dendrite growth and improving the safety of Li metal anodes (LMAs). Among the proposed strategies, depositing an interlayer onto LMA or current collectors for reinforcing SEI formation [7–10] and constructing lithiophilic three-dimensional (3D) conductive frameworks with enlarged surface area on current collectors have emerged as a particularly effective approach [11–14]. Such architecture reduces the nucleation energy barrier, homogenizes current distribution across the electrode, and accelerates charge transport, thereby guiding uniform Li deposition [15–17]. In particular, porous structures provide abundant surface area and interconnected pathways that promote omnidirectional Li plating, effectively suppressing dendrite penetration toward the separator and favoring dense, mossy-like or rounded Li deposits [18–31].

Nevertheless, realizing the current collectors (or Li hosts) that simultaneously satisfy the essential requirements of high lithiophilicity, robust electrical conductivity, and optimal porosity remains a formidable challenge. Moreover, the intrinsic mechanical rigidity of metallic frameworks, coupled with their limited interfacial compatibility, severely restricts their ability to buffer the large volume fluctuations that occur during repetitive Li plating and stripping. These limitations inevitably lead to structural degradation, loss of interfacial stability, and compromised cycling durability. Furthermore, the coupled influence of the lithiophilic surface architecture and the mechanical modulus of current collectors on LMA performance has not yet been investigated, which complicates the rational design of LMA with well-defined and electrochemically effective structures.

Specifically, the Li plating process onto a rigid current collector (e.g., Ni plate with a Young's modulus of ~2.0×10^5 MPa) inevitably induces mechanical and electrochemical stresses that depend on the curvature or shape of the solid-solid interface [32], which significantly influences Li plating behavior in LMB systems [33]. Mechanically compliant or microstructured hosts can partially accommodate these stresses through soft deformation or structural relaxation, effectively reducing localized stress concentrations that would otherwise trigger protrusive dendrite formation. Such stress-relief mechanisms have been demonstrated in a variety of soft current collectors that can deliberately direct Li flux toward low-stress regions [34–37]. Among various substrates for soft current collectors, elastomeric substrates are particularly attractive because their low effective modulus and high deformability enable efficient stress relaxation during repeated Li plating and stripping, thereby mitigating stress accumulation at the Li/electrode interface that can lead to localized current amplification and dendrite formation. However, despite these mechanical advantages, simultaneously imparting both excellent electrical conductivity and high lithiophilicity to elastomers remains a critical challenge, severely limiting their practical application as current collectors in LMAs. Conventional metallization methods—such as sputtering, evaporation, or hydrothermal coating—often generate brittle conductive layers that fracture under deformation and exhibit poor conformality on complex elastomeric surfaces. Alternatively, incorporating conductive fillers into elastomers typically requires high loading levels, which deteriorate mechanical compliance due to poor interfacial interaction between the fillers and elastomer matrix, ultimately negating the fundamental advantages of elastomeric substrates.

Therefore, the development of elastomeric current collectors that simultaneously provide mechanical compliance, high electrical conductivity, high lithiophilicity, and well-defined architectures can provide a transformative pathway toward a broad range of electrochemical applications, including high-performance LMAs.

In this study, we introduce an elastomeric LMA that integrates a dual nano-crumpled/micro-concave structure with a lithiophilic self-assembled monolayer (SAM) (Scheme 1). Additionally, our work highlights how the synergistic integration of elastomeric mechanical compliance, surface architecture, and lithiophilic interfacial chemistry can effectively regulate Li deposition behavior and enhance electrochemical stability of elastomeric metal anodes. Specifically, the hierarchical architecture in elastomeric substrate, together with molecular-level surface functionalization, reduces Li nucleation overpotential, mitigates both mechanical and electrochemical stresses, and suppresses irregular dendrite growth, thereby markedly enhancing cycling stability. To achieve this goal, the micro-cavities were preferentially formed on the elastomer surface by mechanically rubbing monodisperse polystyrene particles, followed by a replica molding process. In parallel, nano-crumpled features were generated on the elastomeric substrate through nonpolar solvent-swelling-induced hydrophobic metal nanoparticle (NP) assembly and polar solvent-deswelling-driven amine linker assembly. This non-destructive, reversible swelling-deswelling behavior of poly(dimethyl siloxane) (PDMS) enables the formation of a highly uniform and stable crumpled structure. Ni was then electrodeposited onto the metal NP-coated elastomer (Ni-PDMS) to improve electrical conductivity. Notably, the resulting high-quality and conformal thin metallic coating effectively retains the intrinsic elastomeric nature of the PDMS substrate while preserving the pre-engineered surface topography without any structural deformations.

As a result, this dual nano/micro-structured metallic elastomer host, with a relatively low elastic modulus of 31.4 MPa, not only relaxes the localized interfacial stresses during Li deposition but also increases the effective surface area. To impart high lithiophilicity, the formed Ni-PDMS surface was additionally deposited with an ultrathin (~0.6 nm) amine (–NH_2)-functionalized tris(2-aminoethyl)amine monolayer (TREN, M_w ~146) through facile

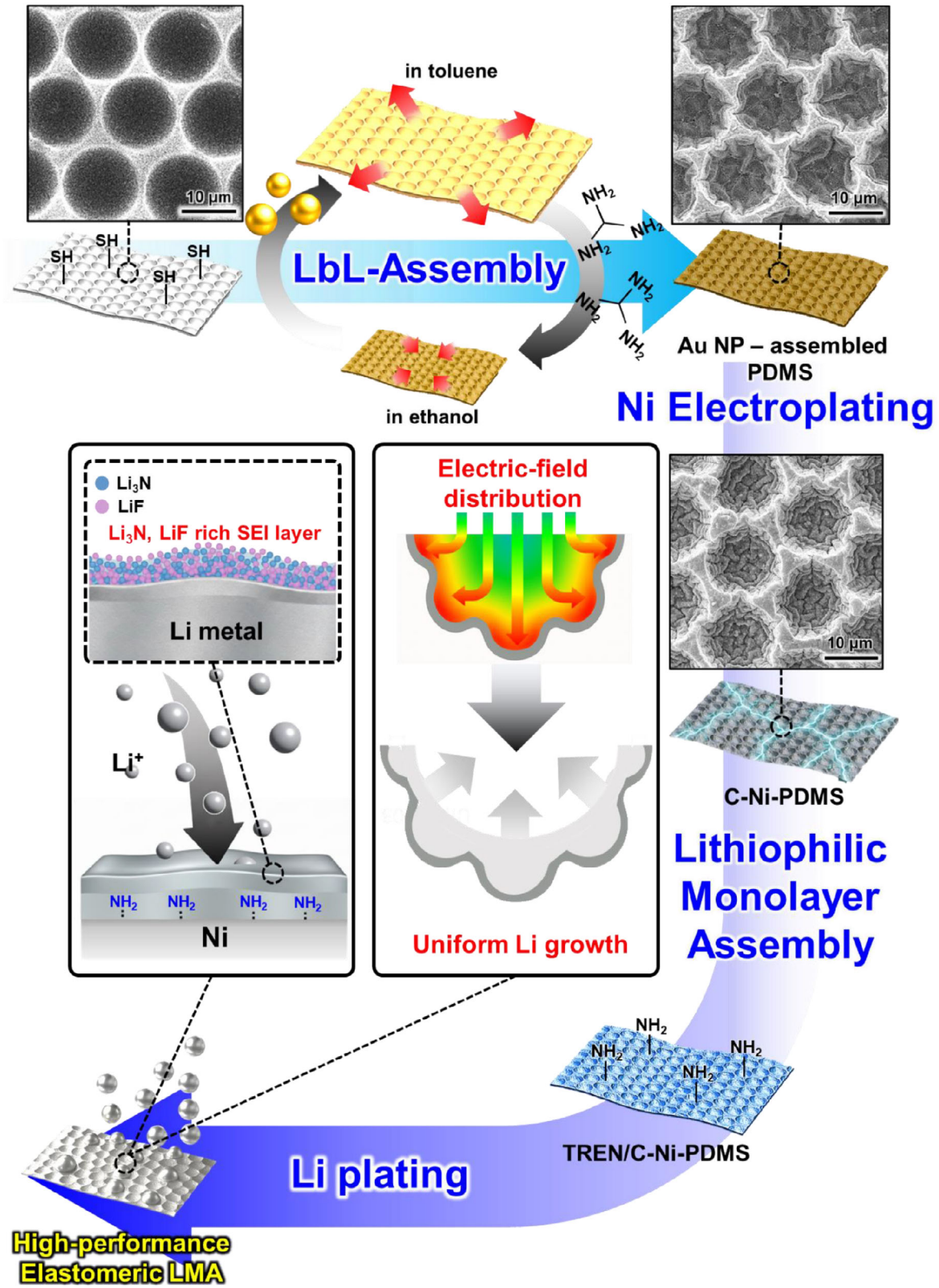

SCHEME 1 | Schematic illustration of the fabrication process and working principle of dual nano-crumpled/micro-concave elastomeric Li host.

SAM process. Unlike bulky polymer coating, this molecular monolayer assembly increases Li affinity without compromising electrical conductivity, thereby suppressing uncontrolled dendritic growth. The synergistic effect of dual structures (nano-crumpled features and micro-cavities) and lithiophilic SAM treatment enlarges the accessible lithiophilic surface area and provides free volume to accommodate deposited Li, ensuring uniform distribution, alleviates stress concentrations, reducing overpotentials (from 124.5 mV for Ni plate to 11.0 mV for TREN-Ni-PDMS at 0.5 mA cm^{-2}), and effectively preventing dendritic

growth. The resulting symmetric cells demonstrated exceptional cycling stability (~2,600 h at 1 mA cm^{-2}/1 mAh cm^{-2} and ~2,170 h at 3 mA cm^{-2}/3 mAh cm^{-2}), significantly outperforming the TREN-free Ni-PDMS electrodes with and without concave structures. In addition, a full-cell configuration composed of the concave-structured LMA and the conventional $LiFePO_4$ (LFP) cathode achieved outstanding cycling stability, retaining 90.2% capacity after 1,000 cycles at 1C.

Although elastomeric current collectors featuring concave or patterned structures have been extensively investigated, elastomeric host electrodes incorporating dual hierarchical architectures fabricated via combined mechanical and solution-based processes have not, to our knowledge, been previously reported. More importantly, this work provides a conceptual advance by demonstrating that such elastomeric electrodes can be effectively applied to high-performance lithium metal anodes.

Therefore, our lithiophilic nano-crumpled/micro-concave elastomeric design offers a robust and versatile platform for achieving dendrite-free and long-term stable operation, thereby establishing a solid foundation for the development of next-generation high-performance lithium metal batteries (LMBs).

2 | Results and Discussion

2.1 | Nano-Crumpled and Flat PDMS Host Electrodes

To develop high-performance elastomeric LMAs, we first fabricated elastomeric host electrodes that feature a large surface area, high electrical conductivity, and excellent mechanical flexibility (Figure 1a). This was achieved through the assembly of metal NPs followed by subsequent metal electroplating. The metal NP assembly was carried out on thiol (SH)-functionalized PDMS with a thickness of approximately 200 μm. In this configuration, the assembled metal NPs act as a conductive seed layer for the subsequent electroplating step. Specifically, tetra(octyl ammonium bromide) (TOABr)-stabilized Au NPs (i.e., Au NPs), with a diameter of ~8 nm in toluene, were densely deposited onto the PDMS surface. This deposition was driven by strong covalent bonding interaction between the bare Au NP surfaces and the SH moieties on the PDMS. During this direct adsorption, the bulky, insulating, and hydrophobic TOABr ligands loosely bound to the surface of Au NPs were effectively removed. To further enhance interparticle connectivity, the remaining TOABr ligands existing on the outer surface of the adsorbed Au NPs were subsequently replaced with the small organic linker molecules (molecular weight (M_w) ~ 146) containing amine (NH_2) groups (i.e., tris(2-aminoethyl)amine, $N(CH_2CH_2NH_2)_3$, TREN) in ethanol. This ligand exchange reaction-induced LbL assembly [38] was confirmed by Fourier transform infrared (FTIR) spectroscopy during LbL assembly of $(Au\ NP/TREN)_n$ multilayers (where n is the number of bilayers) (Figure 1b and Figure S1). Specifically, the TOABr-Au NP-coated substrate (n = 0.5) exhibited distinct characteristic peaks at 2,850–2,960 cm^{-1}, originating from the C−H stretching vibrational modes of the outermost bulky TOABr ligands. These peaks dramatically disappeared after the sequential deposition of the TREN layer onto the Au NP layer, indicating that the TOABr ligands are completely replaced by TREN. This phenomenon was consistently observed with increasing the bilayer number (n), demonstrating an effective ligand exchange reaction during the LbL assembly process. The strong interfacial interaction between the NH_2 groups of TREN and the Au NP surfaces was further validated by the regular, vertical growth of $(Au\ NP/TREN)_n$ multilayers, as confirmed by quartz crystal microbalance (QCM) measurements and UV–vis spectroscopy (Figure 1c and Figure S2). The QCM measurements indicated that each Au NP/TREN bilayer exhibited a linear mass variation (Δm) of about 6.9 μg cm^{-2} (Figure 1c). When the TREN layer was applied onto a substrate already coated with Au NPs, the Δm value showed a slight reduction. This decrease can be attributed to the substitution of the bulky TOABr ligands (M_w ~547) by the much smaller TREN molecules (M_w ~146). This ligand exchange enables the TREN layer to act as a direct molecular bridge between neighboring Au NPs, thereby regulating the interfacial packing density. As shown in Figure 1d, increasing the bilayer number (n) of multilayers from 1 to 3 significantly reduced the sheet resistance of $(Au\ NP/TREN)_n$-PDMS film from ~10^8 to ~88 Ω sq^{-1}, reaching a level suitable for subsequent Ni electroplating to fully metallize the elastomer (Figure S3).

Another notable observation is the hazy, yellowish appearance of the $(Au\ NP/TREN)_n$-PDMS film surface, which is attributed to the formation of a crumpled structure induced by the densely packed Au NP multilayers (Figure 1e). These isotropic crumples emerged after the deposition of the first Au NP/TREN bilayer onto the PDMS substrate, and no significant changes in the crumpled surface morphology were observed thereafter, indicating the uniform growth of the Au NP multilayers. (Figure 1e). The resulting surface crumples exhibited a wavelength of approximately 2.2 ± 0.5 μm and an amplitude of 0.9 ± 0.2 μm, as confirmed by atomic force microscopy (AFM) (Figure 1f). In particular, upon immersion of the swollen Au NP-assembled PDMS film into the ethanol solution for TREN deposition, the PDMS underwent deswelling, returning to its original size. This rapid shrinkage induced a strong lateral compressive stress across the PDMS surface. According to the theory of buckling instability, which occurs when the interfacial compressive stress exceeds a critical threshold [39], the observed crumpling can be attributed to the contraction of the swollen Au NP-assembled PDMS during the ethanol-induced deswelling process. Notably, this structural evolution is not strictly limited to Au NPs and PDMS size. Specifically, Ag- and Cu-based assemblies also formed wrinkled and interconnected NP frameworks through the same LbL assembly process (Figure S4). Additionally, given that our approach is mainly based on solution dipping process, the PDMS electrode size can be easily extended to large size (Figure S5). These results highlight the material versatility and electrode scalability of the proposed approach.

This surface crumples originate from the buckling instability of the $(Au\ NP/TREN)_n$ multilayers, which deform to accommodate the substantial contractive force generated during PDMS deswelling [40]. The characteristic crumple wavelength (λ) on the flat PDMS can be described by the following equation:

$$\lambda = 2\pi T \left(\frac{\bar{E}_f}{3\bar{E}_s}\right)^{1/3} = 2\pi T \left(\frac{\bar{E}_f}{3E_s}\left(1-\nu_s{}^2\right)\right)^{1/3} \quad (1)$$

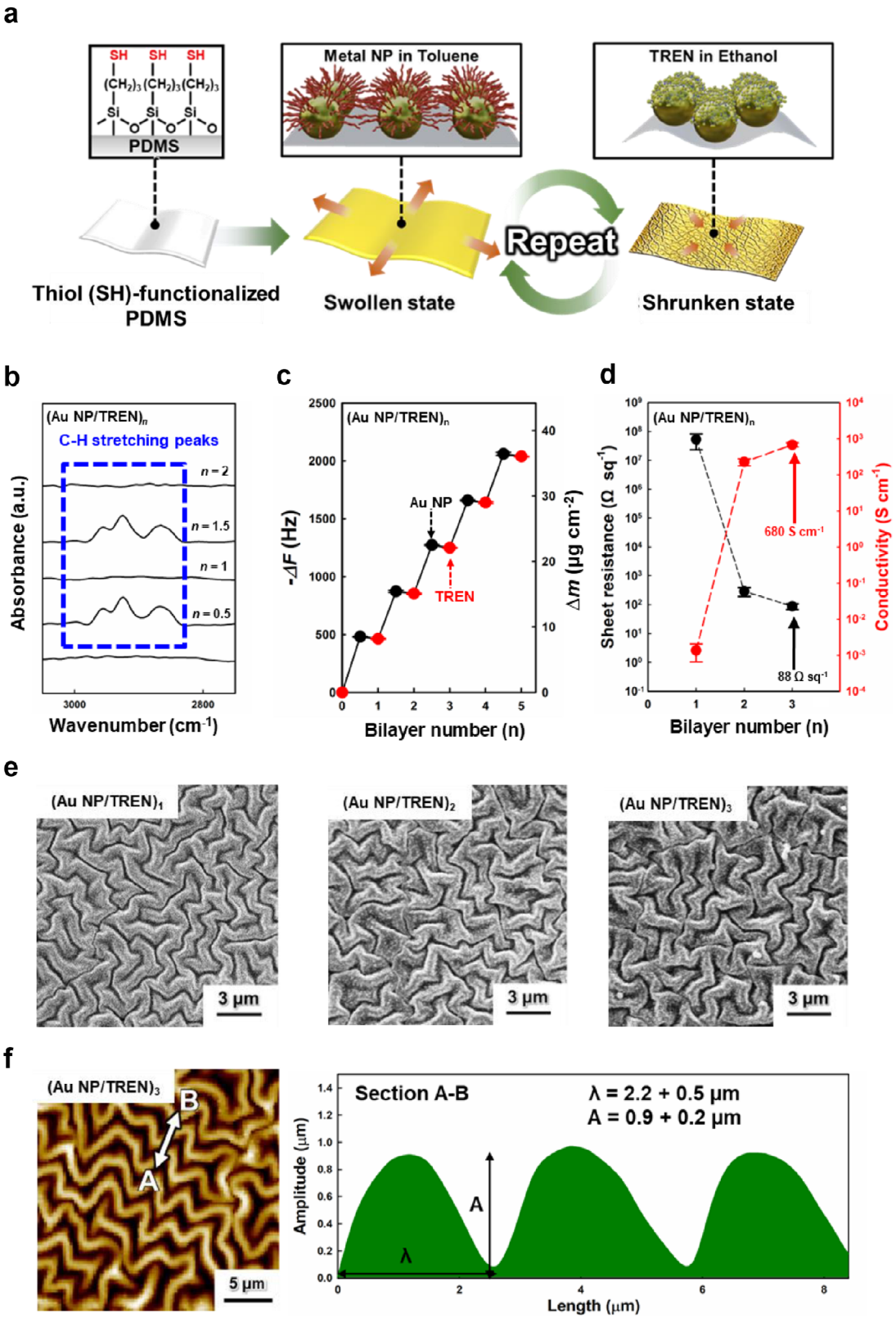

FIGURE 1 | Fabrication of crumpled and conductive PDMS. (a) Schematic illustration for wrinkled elastomeric electrode fabrication. (b) FTIR spectra of $(Au\ NP/TREN)_n$ multilayers as a function of bilayer number (n). (c) QCM analysis of $(Au\ NP/TREN)_n$ multilayers as a function of bilayer number. (d) Change in sheet resistance and electrical conductivity of $(Au\ NP/TREN)_{n\ =1,2,and\ 3}$ multilayers. (e) FE-SEM images of $(Au\ NP/TREN)_{n\ =1,2,\ and\ 3}$-PDMS. (f) AFM images for crumpled morphology (left) and corresponding height profile (right) of $(Au\ NP/TREN)_3$-PDMS, revealing the characteristic wrinkle wavelength (λ) and amplitude (A).

where T is the thickness of the Au NP multilayers, $\bar{E}_f$ is the effective modulus of the Au NP multilayers (the modulus of the inserted TREN molecular linkers is here neglected), E_s is the Young's modulus (~2.4 MPa) of the PDMS, and ν_s (~0.5) is the Poisson's ratio of the PDMS substrate. The Poisson's ratio of PDMS was assumed to be 0.5, based on its well-established near-incompressible elastomeric behavior; a value of 0.48 has also been reported in the literature for related buckling analyses [41]. Since the crumple morphology is essentially determined by the properties of the initial bilayer, both λ and T correspond to the wavelength and thickness of the Au NP layer (approximately ~2.2 μm and ~142 nm, respectively). Using this relationship, the effective modulus $\bar{E}_f$ of the (Au NP/TREN) film was estimated to be approximately 141.2 MPa—significantly lower than the reported Young's modulus (~5.5 × 10^4 MPa) of bulk Au thin films [42].

2.2 | Nano-Crumpled F-Ni-PDMS Host Electrodes

Subsequent Ni electroplating onto the (Au NP/TREN)$_3$-assembled PDMS generated a smooth, continuous metallic layer that faithfully replicated the underlying nano-crumpled morphology, as confirmed by FE-SEM and energy dispersive spectroscopy (EDS) imaging (Figure 2a and Figure S6). Importantly, Ni electroplating enables the formation of a robust, continuous metallic layer onto PDMS surface, fundamentally distinguishing it from typical elastomeric conductors fabricated by depositing discrete metal NPs, where are prone to particle aggregation during electrochemical cycling and consequent degradation of electrical conductivity and electrochemical performance. In general, Ni electrodeposition yields more uniform and stable coatings than Cu due to its more controlled electrochemical kinetics and stronger interfacial interactions with the conductive substrate. Progressive thickening of the electroplated Ni layer led to substantial improvements in electrical conductivity. After only 30 s of electroplating, the sheet resistance rapidly decreased to ~4.0 Ω sq^{-1} (~1.1 × 10^4 S cm^{-1} for conductive Au NP and Ni layers), and extending the deposition to 60 s (Ni thickness ~155 nm) further reduced the resistance to ~0.90 Ω sq^{-1} (~3.6 × 10^4 S cm^{-1} for conductive Au NP and Ni layers). Continued plating for 120 s (Ni thickness ~335 nm) and 180 s (Ni thickness ~490 nm) yielded even lower resistances of ~0.42 Ω sq^{-1} (~4.8 × 10^4 S cm^{-1} for conductive Au NP and Ni layers) and ~0.23 Ω sq^{-1} (~6.7 × 10^4 S cm^{-1} for conductive Au NP and Ni layers), respectively—representing a reduction of more than three orders of magnitude relative to the original (Au NP/TREN)$_3$ seed multilayer (Figure 2b and Figures S7 and S8). Importantly, the FE-SEM observations confirmed that the crumpled morphology of the elastomeric template remained intact at all electroplating times (Figure S9), indicating that electroplating does not distort the underlying architecture (Note: the elastomeric electrodes with a flat but nano-crumpled structure fabricated through the (Au NP/TREN)$_3$ multilayers and Ni electroplating are hereafter referred to as F-Ni-PDMS). The formation of a continuous metallic Ni film was further verified by X-ray diffraction (XRD), which confirmed the presence of well-defined Ni crystallographic features on the Au NP-assembled PDMS surface (Figure S10).

In addition, the structural stability of the elastomeric substrate under practical electrolyte environments was systematically investigated. Bare PDMS, Au–PDMS, and Ni–PDMS exhibited negligible dimensional changes after immersion in 1 M LiTFSI in DOL/DME and 1 M $LiPF_6$ in EC/DMC for 150 h. In contrast, pronounced swelling was observed in toluene, with the sample diameter increasing by approximately 1.3-fold (Figure S11). Furthermore, FE-SEM analysis confirmed that the nano-crumpled morphology of the Ni-coated PDMS was well preserved after electrolyte immersion, with no observable structural collapse, cracking, or delamination.

The mechanical compliance of the F-Ni-PDMS elastomer was evaluated through instrumented nanoindentation (Figure 2c and Figure S12). Reduced moduli were determined from instrumented nanoindentation experiments by applying the Oliver–Pharr method to the unloading segments of the load-displacement curves, yielding values of 22, 24, 39, and 42 MPa for the 30, 60, 120, and 180 s samples, respectively. In the Oliver–Pharr framework, the reduced modulus (E_r) is related to the elastic modulus of the sample (E_s) and the diamond indenter (E_i) through

$$\frac{1}{E_r} = \frac{1-\nu_s^2}{E_s} + \frac{1-\nu_i^2}{E_i}.$$

Because the PDMS-dominated composite is orders of magnitude softer than the diamond indenter (E_i ~1.1 × 10^6 MPa, ν_i ~0.07), the second term is negligibly small and was omitted. Accordingly, the elastic modulus was calculated using simplified relation:

$$E_s \approx \frac{E_r}{1-\nu_s^2},$$

Assuming a Poisson's ratio of 0.50 for the elastomer-supported hybrid electrode, the resulting elastic moduli (E_s) were estimated to be approximately 29.3, 31.4, 52.5, and 55.7 MPa, respectively [43]. The 30 s sample exhibited the lowest modulus, reflecting an ultrathin, highly deformable Ni layer that remained intimately coupled to the elastomeric substrate. Increasing the plating time to 60 s resulted in a slightly higher modulus, yet the electrode remained mechanically compliant. In contrast, the 120 s and 180 s samples exhibited substantially larger stiffness owing to the increased Ni thickness and progressive densification of the metallic network. These results confirm that thin Ni coatings with a thickness of ~155 nm (electroplating time 60 s) preserve elastomer-like mechanical compliance, exhibiting high electrical conductivity, whereas excessive electroplating leads to pronounced stiffening of the hybrid electrode.

Additionally, this mechanically induced evolution directly affected the durability of the electrodes under repeated deformation. In cyclic bending tests (radius = 1.3 mm), the 30 and 60 s electrode maintained remarkably stable resistance over 20 000 cycles, whereas the 120 and 180 s electrodes exhibited pronounced resistance increases, reflecting their reduced flexibility and greater susceptibility to microcrack formation (Figure S13a). Consistent trends were observed under 150% uniaxial stretching. Only the 30 and 60 s electrodes remained mechanically intact, whereas the 120 s (Ni film thickness ~335 nm) and 180 s samples (Ni film thickness ~490 nm)

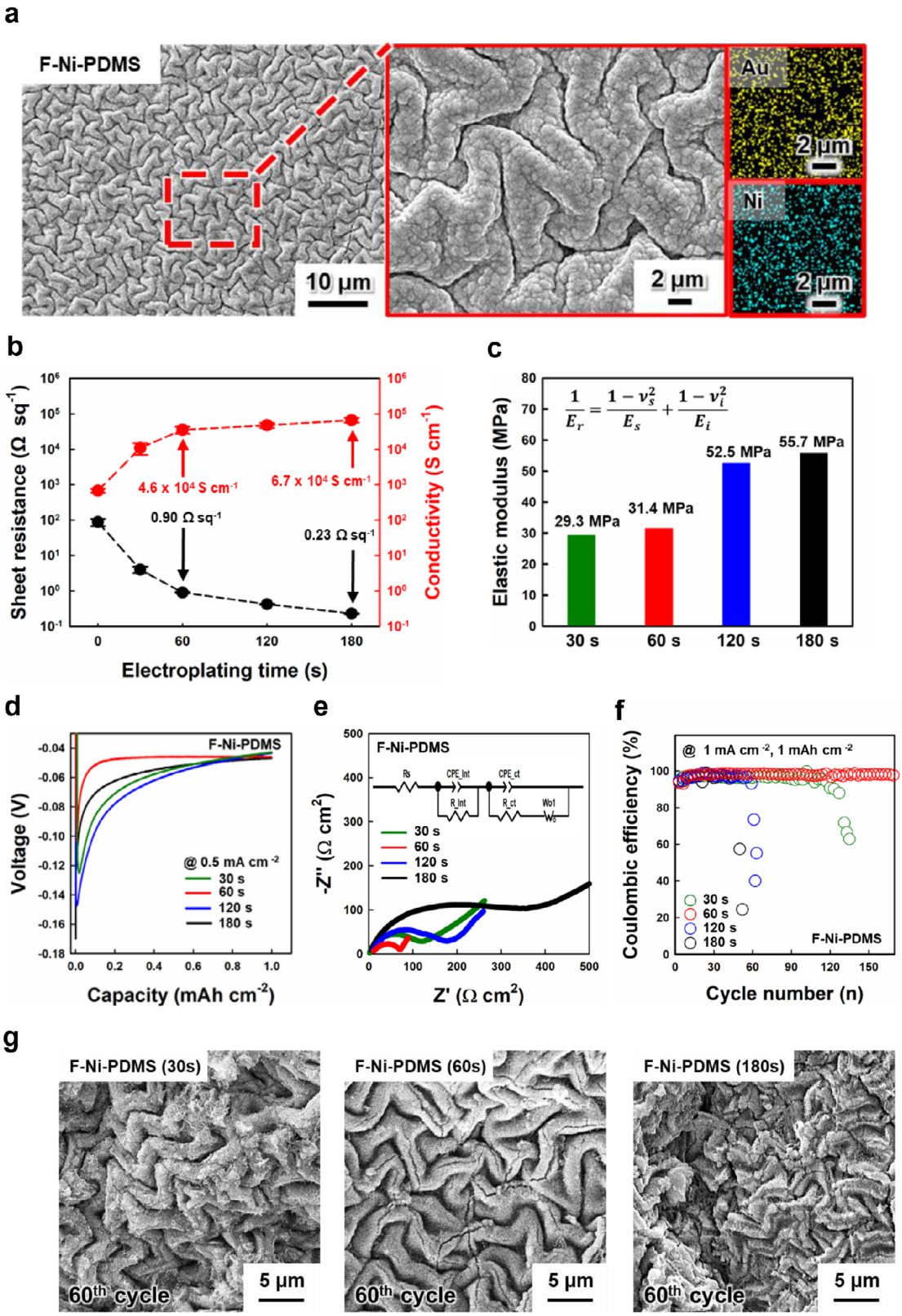

FIGURE 2 | The mechanical and electrochemical properties of F-Ni-PDMS. (a) FE-SEM images of F-Ni-PDMS and corresponding EDS elemental mapping. (b) Sheet resistance and conductivity as a function of Ni electroplating time. (c) Elastic moduli of F-Ni-PDMS electrodes with different Ni electroplating times. (d) Voltage-capacity profiles during Li nucleation at 0.5 mA cm^{-2} for electrodes prepared with different Ni electroplating times. (e) Nyquist plots from EIS analysis of F-Ni-PDMS with varying Ni electroplating time. The inset shows the equivalent circuit. (f) Coulombic efficiency of half-cells during Li plating/stripping at 1 mA cm^{-2} and 1 mAh cm^{-2}. (g) Top-view FE-SEM images of F-Ni-PDMS electrodes after 60 Li plating/stripping cycles (at 1 mA cm^{-2} and 1 mAh cm^{-2}).

fractured at the onset of deformation (Figure S13b). Notably, the 60 s electrode, with an optimized Ni film thickness of ~150 nm, maintained nearly constant resistance during repeated stretching cycles. By comparison, the 30 s electrode exhibited a gradual resistance increase, which can be attributed to progressive mechanical degradation arising from its considerably thinner Ni film (~80 nm).

Notably, the mechanical transition also exerted a pronounced influence on electrochemical behavior. During Li plating at 0.5 mA cm^{-2}, the 60 s electrode exhibited the lowest nucleation overpotential (58.0 mV) and the fastest voltage stabilization, consistent with its ability to accommodate interfacial strain and suppress stress-induced Li irregularities (Figure 2d). Although the 30 s sample is the most compliant, its higher sheet resistance and incomplete metallic coverage still result in a moderately elevated nucleation overpotential (80.0 mV). In contrast, the 60 s sample provides both continuous electrical pathways and mechanical compliance, yielding the lowest nucleation barrier. The 120 and 180 s electrodes with longer electroplating time exhibited substantially higher nucleation overpotentials (97.1 and 123.5 mV, respectively). This trend suggests that reduced mechanical compliance leads to increased interfacial stress and more heterogeneous current distribution during Li nucleation, thereby raising the energetic barrier for Li deposition rather than allowing smooth interfacial accommodation.

Electrochemical impedance spectroscopy (Figure 2e) further supported this trend. The 60 s electrode displayed the lowest interfacial resistance, whereas the thicker electrodes exhibited progressively larger charge-transfer resistances, attributable to their increased stiffness and restricted Li-ion flux. The 30 s electrode suffers from insufficient metallic connectivity, while the 120 s and 180 s samples are penalized by excessive stiffness. In contrast, the 60 s Ni coating forms a more continuous and electronically well-connected metallic skin while still retaining mechanical compliance, thereby enabling more homogeneous Li nucleation and improved interfacial stability.

As a direct consequence of these interfacial and mechanical differences, the electrodes exhibited distinctly different cycling stabilities (Figure 2f). The 60 s F-Ni-PDMS electrode delivered excellent Coulombic efficiency and maintained its crumpled morphology over extended cycling, whereas the 120 s and 180 s electrodes experienced rapid efficiency decay accompanied by severe surface roughening and dendritic Li deposition. Consistent with these trends, the FE-SEM analysis after 60 cycles (Figure 2g) revealed that the nano-crumpled framework was largely preserved in both the 30 s and 60 s electrodes, while the 180 s electrode exhibited pronounced morphological collapse and irregular Li accumulation. With further cycling to 120 cycles, the 60 s electrode still retained its crumpled architecture, whereas the 30 s electrode began to develop fragmented and partially disrupted metallic domains (Figure S14). These results demonstrate that a mechanically compliant thin-Ni architecture offers the optimal balance among electrical conductivity, mechanical durability, and interfacial electrochemical stability, highlighting the critical role of host stiffness in governing LMA performance [36].

2.3 | Nano-Crumpled and Micro-Concave-Structured PDMS Host Electrodes

Based on these results, we fabricated PDMS host electrodes incorporating both crumpled and concave structures to enlarge the electrochemically active surface area. To generate the concave geometry, 15 μm dry polystyrene (PS) colloids were mechanically rubbed onto PDMS-coated substrates using another rubbery substrate [44, 45]. During this process, the colloids were successfully transferred to the PDMS surface. Following the transfer, the PS colloids spontaneously assembled into hexagonally close-packed monolayers on both rubbery substrates, which were then employed as molds to create PDMS replica with a well-defined micro-concave structure (Figure 3a; Detailed Experimental Section, Supporting Information).

To impart the electrical conductivity to the concave-structured PDMS and further increase its surface area, the $(Au\ NP/TREN)_{n\ =\ 1,2,\ and\ 3}$ multilayers were uniformly deposited onto the concave-structured PDMS (Figure S15), followed by Ni electroplating. This sequence yielded a highly conductive nano-crumpled and micro-concave PDMS host (hereafter referred to as C-Ni-PDMS). The FE-SEM and EDS mapping images confirmed the conformal deposition of both the $(Au\ NP/TREN)_3$ multilayers and the electroplated Ni across the entire surface (Figure 3b). The cross-sectional FE-SEM further revealed that Ni coated the interior of the concave cavities with thickness identical to that on the top surfaces (Ni electroplating time ~60 s), demonstrating uniform metal deposition even on concave regions (Figure S16). The formation of nanoscale crumples within the micrometer-scale concave features generated a hierarchical micro-nano architecture expected to significantly increase accessible electrochemical surface area.

This enhancement was quantitatively validated using cyclic voltammetry (CV) in the non-Faradaic region (0.85–0.95 V vs. RHE). As shown in Figure S17, the C-Ni-PDMS electrodes exhibited the highest electric double-layer capacitance (C_{edl}) and the largest electrochemically active surface area (ECSA, 27 cm^2). In contrast, Au-sputtered concave PDMS—lacking nanoscale crumple features—showed much lower ECSA values (Figure S18), underscoring the critical role of nano-crumpling.

To clarify the structural influence on ionic transport and electric-field distribution, electrolyte current-density profiles were simulated using COMSOL under an applied current density of 0.5 mA cm^{-2} (Figure 3c and Figure S19). While a planar Ni plate produced uniform and vertical ionic flux, the F-Ni-PDMS electrode displayed moderate lateral deflection due to nanoscale corrugation. In contrast, the C-Ni-PDMS electrode induced deep penetration of current lines into the concave cavities and guided them uniformly along the crumpled interiors, effectively mitigating the rim-focusing effect typical of non-crumpled concave electrodes.

These structural merits were directly reflected in the enhanced electrochemical performance. As shown in Figure 3d, the C-Ni-PDMS exhibited the lowest Li nucleation overpotential (21.4 mV), reflecting reduced local current density and improved ionic accessibility during initial plating. Notably, even F-Ni-PDMS—with nanoscale crumples but no concavity—achieved substantially

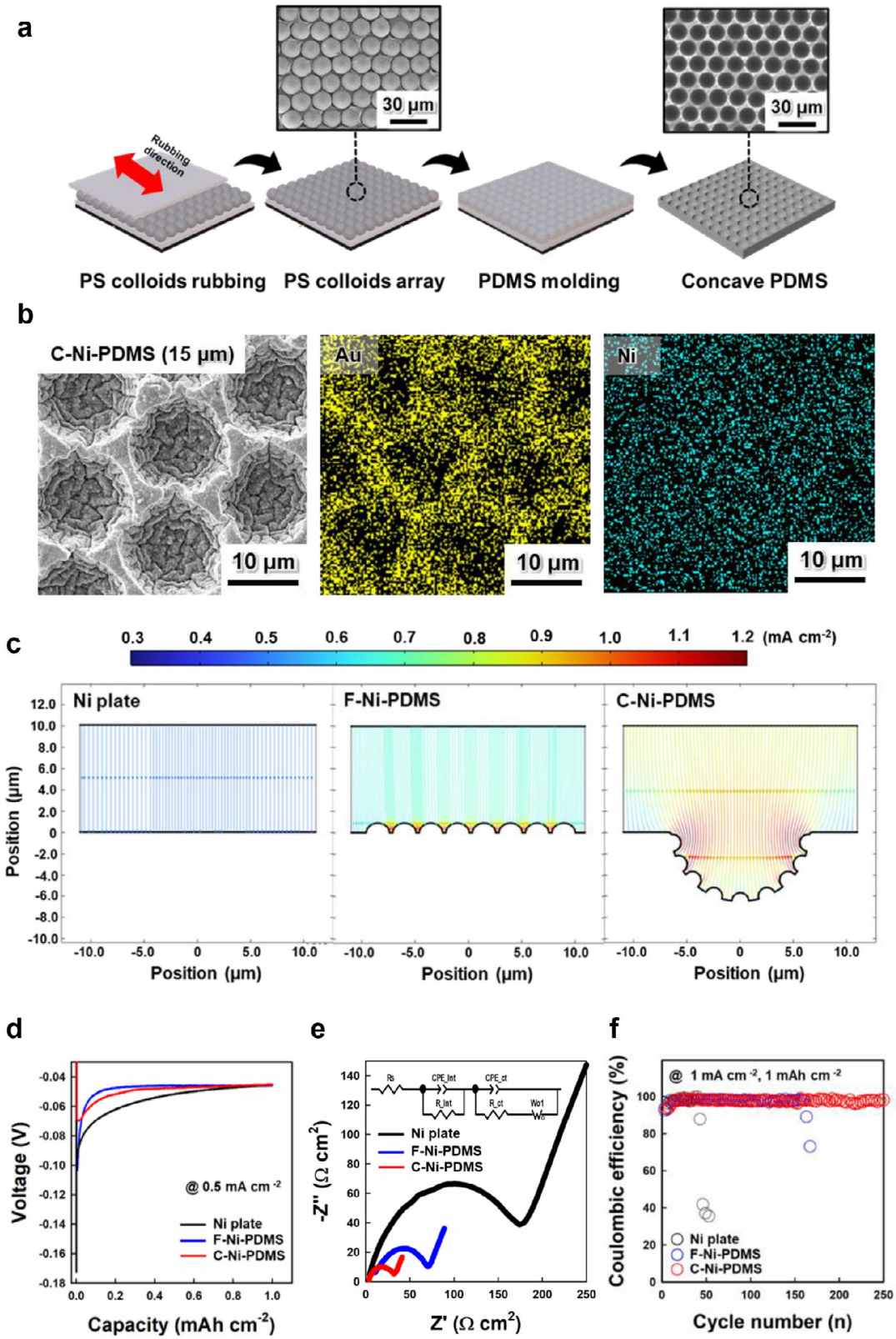

FIGURE 3 | Electrochemical properties of C-Ni-PDMS. (a) Schematic illustration for fabricating concave PDMS. (b) FE-SEM image and corresponding EDS elemental mapping of C-Ni-PDMS. (c) COMSOL simulation showing the electrolyte current density distribution for the different electrode structures. (d) Voltage-capacity curves of Ni plate, F-Ni-PDMS and C-Ni-PDMS during Li nucleation at 0.5 mA cm^{-2}. (e) Nyquist plots from EIS analysis of Ni plate, F-Ni-PDMS, and C-Ni-PDMS. The inset shows the equivalent circuit. (f) Coulombic efficiency of half-cells employing Ni plate, F-Ni-PDMS, and C-Ni-PDMS during Li plating/stripping at 1 mA cm^{-2} and 1 mAh cm^{-2}.

lower overpotential than a flat Ni plate, highlighting the benefit of nanoscale roughness. In contrast, the Au-sputtered concave PDMS, which possesses only micro-concavity without nanoscale crumpling, showed a much higher overpotential (83.2 mV), confirming that the presence of a nano-crumpled structure as well as a micro-concave structure plays an important role in promoting uniform Li nucleation (Figure S20).

Electrochemical impedance spectroscopy (Figure 3e and Figure S21) further demonstrated that C-Ni-PDMS possessed the smallest interfacial resistance and charge-transfer impedance, fully consistent with its enlarged ECSA and highly accessible hierarchical surface. These features led to exceptional cycling stability: C-Ni-PDMS maintained nearly 100% Coulombic efficiency for over 250 cycles at 1 mA cm^{-2} and 1 mAh cm^{-2}, whereas the Ni plate, F-Ni-PDMS, and Au-sputtered concave PDMS exhibited early failure (Figure 3f and Figure S22). The cross-sectional FE-SEM imaging of the C-Ni-PDMS electrode after plating 1 mAh cm^{-2} of Li at 0.5 mA cm^{-2} confirmed the formation of a uniform, dense, dendrite-free Li morphology conformally deposited along the interior of concave structures. This observation provides direct visual evidence that the crumpled-concave architecture effectively guides Li deposition while preserving interfacial integrity, in contrast to the nonuniform Li growth observed within the Au-sputtered concave Ni-PDMS cavities (Figure S23). These results evidently demonstrate that the synergistic integration of nanoscale crumpling and microscale concavity as well as the modulus of elastomer host is essential for lowering nucleation barriers, minimizing interfacial resistance, and achieving highly reversible Li plating/stripping on elastomeric current collectors.

2.4 | Electrochemical Property of lithiophilic TREN/C-Ni-PDMS Electrode

To further transform the C-Ni-PDMS into a highly lithiophilic host, an additional solution-based surface treatment was conducted using the same TREN ($N(CH_2CH_2NH_2)_3$), which served as a molecular linker bridging adjacent Au NPs (Figure S24a). Nitrogen-containing functional groups such as $–NH_2$ are well known to strongly interact with Li through their lone pair electrons, which coordinate with Li^+ ions and stabilize the surface during nucleation process [46, 47]. In particular, the TREN provides multiple nitrogen sites that can simultaneously bind Li^+ ions, thereby forming a dense lithiophilic network on the Ni surface. The simple and mild solution-based SAM process yielded a uniform, conformal TREN monolayer on the Ni surface via strong covalent bonding, without altering the electrical conductivity of the C-Ni-PDMS (Figure S24b). The EDS mapping images also demonstrated a conformal distribution of the $–NH_2$ groups across both the outer and concave regions of the structure (Figure S24c).

The successful formation of the lithiophilic monolayer was further validated by X-ray photoelectron spectroscopy (XPS), which revealed characteristic nitrogen-related signals consistent with TREN binding (Figure S25). Importantly, the presence of surface-bound $–NH_2$ groups significantly enhanced electrolyte affinity, reducing the contact angle from ~35° for pristine C-Ni-PDMS to ~17° for TREN/C-Ni-PDMS (Figure S26). Enhanced wettability facilitates homogeneous electrolyte infiltration into the hierarchical crumpled-concave structures, thereby homogenizing local Li^+ flux. As a direct consequence of this improved interfacial environment, the TREN/C-Ni-PDMS electrode exhibited a substantially reduced Li nucleation overpotential of 11.0 mV at 0.5 mA cm^{-2}, compared to 21.4 mV for unmodified C-Ni-PDMS (Figure 4a). The lower overpotential reflects a reduced energetic barrier for nucleation arising from enhanced Li^+ affinity and improved surface homogenization.

To mechanistically account for these improvements, Density Function Theory (DFT) calculations were performed to elucidate the effect of TREN on the adsorption of electrolyte components at the $Ni(OH)_2$ surface (see Figure S27a) of the electroplated Ni layer. As an initial step, the adsorption energy of a single TREN molecule on the pristine $Ni(OH)_2$ surface was calculated, yielding a stable adsorption energy of −0.84 eV (Figure S27). This confirms the thermodynamic favorability of TREN binding to the surface. As illustrated in Figure 4b, the assembled TREN layer profoundly modulates the surface affinity toward electrolyte species. Specifically, it slightly enhances Li^+ adsorption, thereby improving the lithiophilicity of the $Ni(OH)_2$ surface and lowering the Li nucleation barrier. More importantly, TREN modification markedly strengthens the adsorption of anions (NO_3^- and $TFSI^-$) of electrolytes by approximately 0.2–0.3 eV, whereas the adsorption changes for solvent molecules (e.g., 1,2-dimethoxyethane (DME) and 1,3-dioxolane (DOL)) is relatively minor (~0.1 eV). These results indicate that anions preferentially adsorb on the TREN-assembled surface. To further investigate the interfacial interactions, charge density difference (CDD) analyses were performed. The degree of charge redistribution for the $TFSI^-$ anion was substantially greater than that for solvent molecules such as DME and DOL (Figures S28 and S29), corroborating the enhanced interfacial coupling between anions and the TREN-assembled surface. Overall, the CDD profiles and adsorption energy trends demonstrate that TREN molecules effectively promote both lithiophilic behavior and anion-selective adsorption, thereby contributing to more stable and uniform interfacial environments.

Consistent with this analysis, electrochemical impedance spectroscopy (EIS) demonstrated markedly accelerated interfacial charge-transfer kinetics after TREN functionalization. As shown in Figure 4c, the equivalent series resistance (ESR) values of C-Ni-PDMS and TREN/C-Ni-PDMS are nearly identical, indicating that the bulk ohmic resistance remains largely unchanged upon TREN treatment. In contrast, the charge-transfer resistance (R_{ct}) at the electrode–electrolyte interface is significantly reduced to approximately 14.0 Ω·cm^2 for TREN/C-Ni-PDMS, which is nearly half of that of the untreated C-Ni-PDMS (~28.4 Ω·cm^2). This pronounced reduction indicates facilitated interfacial Li^+ transport, originating from improved wettability (see Figure S26), enhanced electrolyte accessibility, and more favorable interfacial adsorption energetics induced by the TREN monolayer (see Figures S25–S29).

In LMB systems, the Li^+ diffusion coefficient (D), which represents the rate at which ions migrate through the electrolyte and across the electrode interface, plays a crucial role in the formation and stabilization of the SEI layer. As shown in Figure 4d, the Li^+ ion diffusion coefficients for the Ni plate, C-Ni-PDMS, and TREN/C-Ni-PDMS electrodes were calculated to be 0.2×10^{-12},

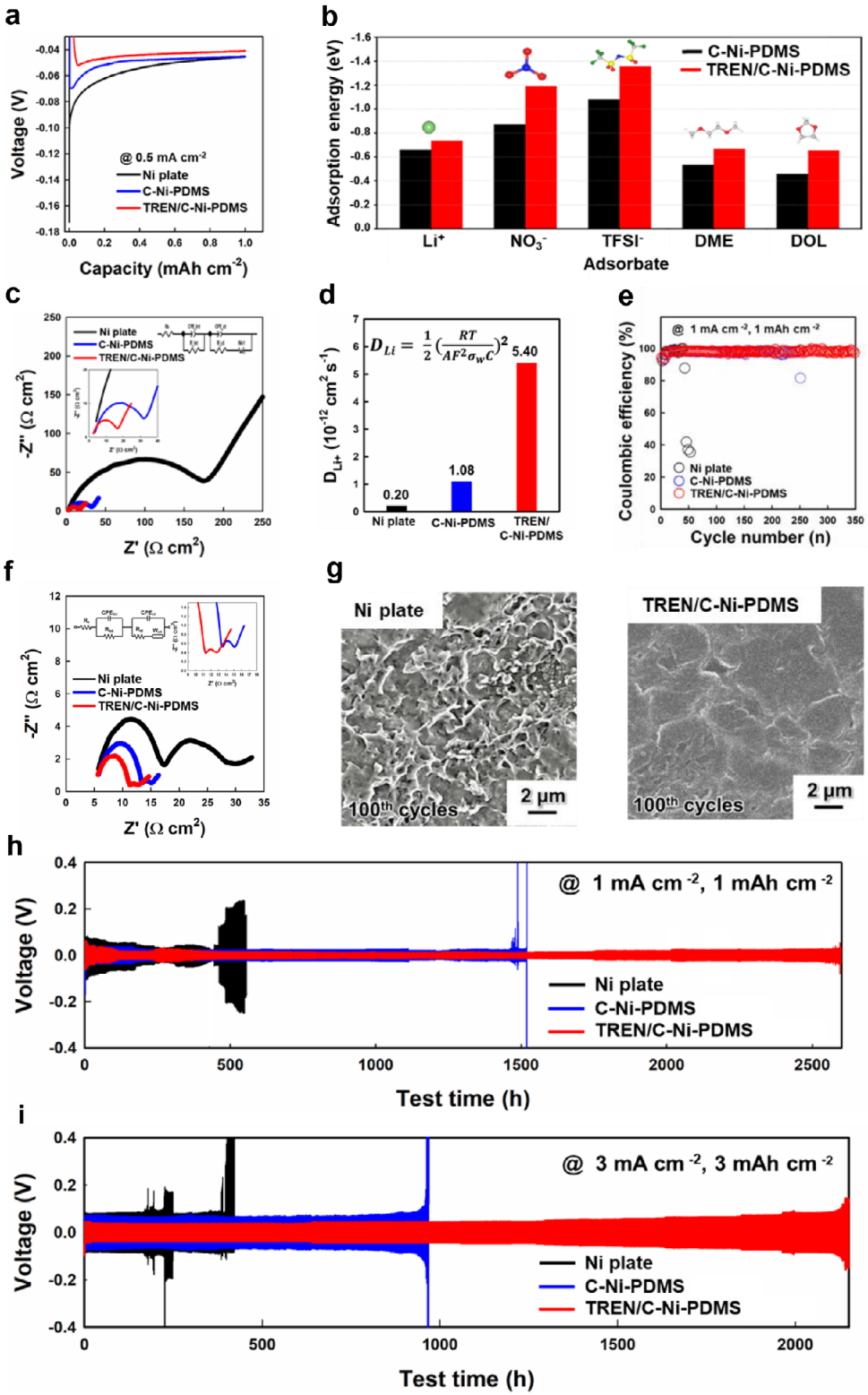

FIGURE 4 | Electrochemical properties of TREN assembled C-Ni-PDMS. (a) Voltage-capacity curves during Li nucleation at 0.5 mA cm^{-2}. (b) The calculated adsorption energies of Li^+, anions (NO_3^- and $TFSI^-$), and solvent molecules (DME and DOL) on $Ni(OH)_2$ and TREN/$Ni(OH)_2$ surfaces. In this case, more negative adsorption energy indicates stronger binding. (c) Nyquist plots of the three different electrodes. The insets show magnified the high-frequency region and the corresponding equivalent circuit. (d) Li-ion diffusion coefficients (D_{Li+}) extracted from the Warburg region of EIS data in c). (e) Coulombic efficiencies of three different half-cells during Li plating/stripping at 1 mA cm^{-2} and 1 mAh cm^{-2}. (f) Nyquist plots of C-Ni-PDMS, TREN/C-Ni-PDMS, and Ni plate symmetric full cells. The insets show enlarged impedance curves in the low-frequency region and the representative equivalent circuit. (g) FE-SEM images of Ni plate (left) and TREN/Ni-PDMS (right) after 100 cycles at 1 mA cm^{-2} and 1 mAh cm^{-2}. Galvanostatic cycling of Li symmetric cells with Ni plate, C-Ni-PDMS and TREN/C-Ni-PDMS at (h) 1 mA cm^{-2} / 1 mAh cm^{-2} and (i) 3 mA cm^{-2} /3 mAh cm^{-2}.

1.08×10^{-12}, and 5.40×10^{-12} cm^2 s^{-1}, respectively. Notably, the TREN modification led to a notable enhancement in ion diffusivity, indicating that the lithiophilic NH_2 groups and modified interfacial environment significantly facilitate Li^+ transport. As a result, the TREN/C-Ni-PDMS electrode exhibited significantly improved cycling stability, maintaining a CE of 98.7% over 350 cycles at 1 mA cm^{-2} and 1 mAh cm^{-2}—well beyond the 250 cycles achieved by the TREN-free C-Ni-PDMS (Figure 4e). Therefore, the pronounced increase in *D* value highlights the synergistic effect of the crumpled-concave PDMS architecture and lithiophilic TREN assembly in optimizing interfacial ion transport, thereby ensuring excellent electrochemical reversibility and long-term cycling stability through effective suppression of Li dendrite formation (Figure S30).

Furthermore, the Ni layer provides critical interfacial electrochemical advantages [48]. The native oxide layer (primarily $NiO/Ni(OH)_2$) formed on the Ni surface acts as an electrochemically active interface that can effectively interact with electrolyte species. In particular, NiO exhibits an optimal binding affinity toward nitrate species, along with a relatively low overpotential for nitrate-related redox reactions. Consequently, this native NiO layer facilitates the preferential reduction of $LiNO_3$ in the electrolyte, thereby promoting the formation of a robust solid electrolyte interphase (SEI) enriched with Li_3N- and LiN_xO_y species, which plays a crucial role in stabilizing Li deposition. Building upon this intrinsic catalytic advantage of the Ni substrate, the subsequent interfacial engineering with TREN further promotes the formation of a more uniform, inorganic-rich SEI layer. Such an SEI is essential for enabling efficient Li^+ transport while simultaneously mitigating parasitic side reactions with the electrolyte [49]. To verify this, the SEI chemical composition of Li anodes based on C-Ni-PDMS and TREN/C-Ni-PDMS electrodes was analyzed by XPS after 10 cycles at 1 mA cm^{-2} in a symmetric cell where 10 mAh cm^{-2} of Li was pre-deposited onto the electrodes before cycling. (Figure S31). In comparison to the untreated electrode, the TREN/C-Ni-PDMS sample exhibited a substantially higher fraction of inorganic SEI constituents, including Li_3N and LiF, accompanied by a marked suppression of organic carbonate species. This inorganic-rich SEI is known to possess higher mechanical robustness and greater Li^+ conductivity, resulting in fewer parasitic decomposition pathways and a more stable electrode/electrolyte interface. This compositional shift toward an inorganic-rich SEI is consistent with enhanced interfacial stability and improved Li^+ transport observed electrochemically.

To further assess the influence of this optimized SEI on interfacial resistance, EIS measurements were conducted after 10 galvanostatic cycles at 1 mA cm^{-2} and 1 mAh cm^{-2} (Figure 4f and Figure S32). Compared to the Ni plate and the C-Ni-PDMS electrodes, the TREN/C-Ni-PDMS electrode showed lower SEI resistance (R_{SEI}) and R_{ct}, indicating enhanced Li^+ ion mobility and improved interfacial charge transfer kinetics. This reduction in resistance is consistent with XPS results, which revealed a higher content of inorganic-rich SEI components (e.g., LiF and Li_3N) known to facilitate rapid Li^+ ion transport. Furthermore, after 100 cycles, the TREN/C-Ni-PDMS electrode displayed more stable and uniform Li deposition than either the Ni plate or the C-Ni-PDMS (Figure 4g and Figure S33a). This improved morphological stability is attributed to the synergistic effect of the crumpled-concave architecture of soft elastomer and lithiophilic TREN assembly, which together promote uniform nucleation and relieve localized stress during repeated cycling. That is, Li was more evenly accommodated within the surface features of TREN/C-Ni-PDMS, effectively suppressing dendritic growth and producing dense, mossy-like deposits. This stabilizing effect persisted even over extended cycling. More specifically, after 600 plating/stripping cycles, the TREN-free C-Ni-PDMS electrode exhibited severe morphological degradation, characterized by irregular Li agglomerates. In contrast, the TREN/C-Ni-PDMS electrode retained a comparatively smooth and compact Li morphology with minimal structural disruption (Figure S33b). As a result, these observations clearly indicate that the simple TREN assembly plays a critical role in maintaining uniform Li deposition throughout prolonged cycling, thereby preventing Li accumulation and surface roughening at the electrode interface.

Based on these findings, the cycling stability was further assessed in symmetric cells based on Ni plate, C-Ni-PDMS, and TREN/C-Ni-PDMS electrodes, and operated at 1 mA cm^{-2} and 1 mAh cm^{-2} (Figure 4h). Bare Ni plate-based cells exhibited early voltage fluctuations and instability, whereas the C-Ni-PDMS symmetric cell maintained a low and stable overpotential for more than 1,400 h, indicating uniform Li plating/stripping. Remarkably, the TREN/C-Ni-PDMS electrodes showed even greater interfacial stability, sustaining smooth voltage profiles for over 2,600 h under the same conditions. Furthermore, the TREN/C-Ni-PDMS electrodes demonstrated excellent durability under more demanding conditions, operating stably for 2,170 h at 3 mA cm^{-2}/3 mAh cm^{-2} and for 500 h at 5 mA cm^{-2} and 1 mAh cm^{-2} (Figure 4i and Figures S34 and S35). These results underscore the critical role of TREN in stabilizing the Li/electrolyte interface under both standard and high-stress cycling conditions.

2.5 | Electrochemical Performance of LFP Cathode-Based Asymmetric Full Cell

To more accurately assess the practical performance of the Li-plated TREN/C-Ni-PDMS anodes (hereafter referred to as 'Li-TREN/C-Ni-PDMS'), asymmetric full-cells were assembled with an LFP cathode (mass loading: 2.64 mg cm^{-2}) and a standard carbonate electrolyte (1 M $LiPF_6$ in EC/DMC with FEC), and subjected to GCD cycling at 1C within a voltage window of 2.5–3.9 V (Figure 5a). In this case, the Li-TREN/C-Ni-PDMS//LFP full-cells exhibited outstanding cycling stability, retaining ~90.2% of their initial capacity after 1,000 cycles, while maintaining an extremely high and stable Coulombic efficiency approaching 100%. In contrast, the C-Ni-PDMS full-cells showed a sharp capacity decline after 500 GCD cycles, indicative of dendrite-induced internal short-circuit failure (Figure S36). Notably, the Li-TREN/C-Ni-PDMS//LFP full-cells also demonstrated stable cycling performance under high-rate conditions at 5C (Figure S37). Furthermore, such stable electrochemical performance was maintained even under elevated temperature conditions, indicating robust interfacial stability against thermally induced degradation (Figure S38). In alignment with our impedance analysis, the TREN-mediated interfacial chemistry plays a key role in suppressing thermally accelerated parasitic reactions while facilitating highly efficient charge-transfer and Li^+ transport kinetics. Additionally, the engineered electrode morphology

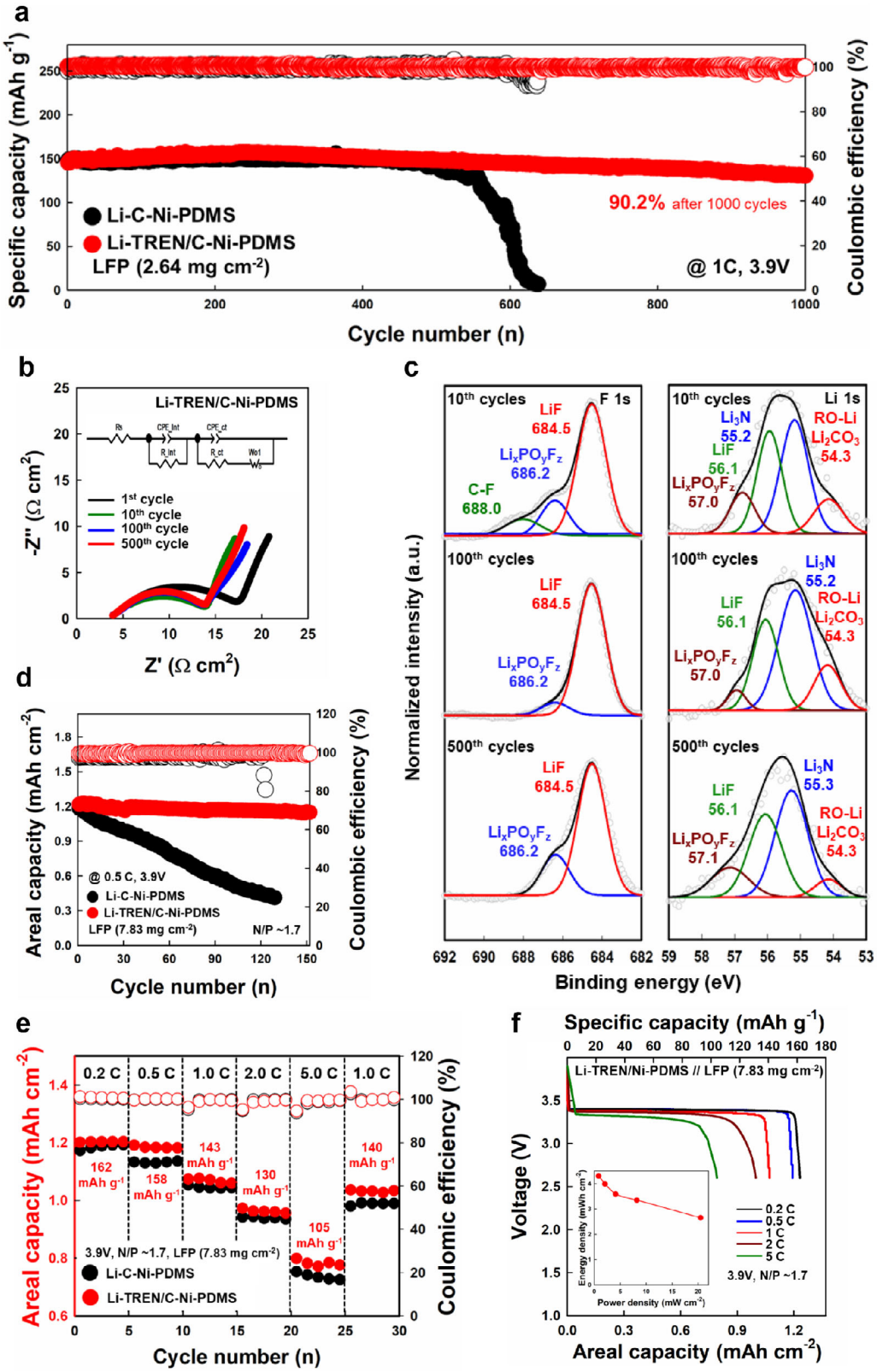

FIGURE 5 | Electrochemical performance of asymmetric full cell. (a) Cycling performance (specific capacity and Coulombic efficiency) of Li-C-Ni-PDMS and Li-TREN/C-Ni-PDMS// LFP (2.64 mg cm^{-2}) at 1C and 3.9 V. (b) Nyquist plots for the Li-TREN/C-Ni-PDMS // LFP full cell after the first, 10th, 100th, and 500th cycles. The inset shows an equivalent circuit. (c) High-resolution XPS spectra (F 1s and Li 1s regions) of the Li-TREN/C-Ni-PDMS surface at 10th, 100th, and 500th cycles. (d) Cycling performance (specific capacity and Coulombic efficiency) of Li-C-Ni-PDMS and Li-TREN/C-Ni-PDMS full cells paired with high-loading LFP (7.83 mg cm^{-2}) at 0.5C and 3.9 V (N/P ratio ~1.7). (e) Rate capability of Li-C-Ni-PDMS//LFP and Li-TREN/C-Ni-PDMS//LFP full cells with a high-loading LFP cathode (7.83 mg cm^{-2}) at various C-rates from 0.2C to 5.0C. (f) Galvanostatic charge–discharge voltage profiles of the full cell at corresponding C-rates. The inset shows Ragone plot of energy density vs. power density.

further enhances performance by promoting more uniform lithium deposition and alleviating localized stress accumulation during repeated cycling. Consequently, stable electrochemical reversibility is effectively maintained across a broad operating temperature range. These results suggest that optimized morphology and interfacial chemistry can effectively sustain interfacial stability and Li^+ ion transport.

The interfacial stability of the Li-TREN/C-Ni-PDMS system was further examined through self-discharge analysis by monitoring the open-circuit voltage (OCV) profiles at room temperature after full charging (Figure S39). The Li-TREN/C-Ni-PDMS // LFP full-cells successfully prevented severe initial voltage loss, maintaining a highly stable OCV of ~3.46 V even after a prolonged rest of 120 h. This outstanding structural stability translated to an exceptional capacity retention of ~99.6% upon subsequent discharge, indicating strongly suppressed parasitic reactions and stable electrode/electrolyte interfaces.

In contrast, the C-Ni-PDMS-based full-cells suffered from a rapid initial voltage drop down to 3.40 V due to severe early-stage parasitic reactions, resulting in a degraded capacity retention of ~96%. These results confirm that the incorporation of the lithiophilic TREN layer not only enhances cycling reversibility but also effectively mitigates self-discharge-induced degradation, thereby reinforcing the reliability of the full-cell performance.

Additional insight into electrochemical abuse tolerance was obtained through overcharge testing of anode-free full cells employing the TREN/C-Ni-PDMS and Cu plate current collectors (Figure S40). In this evaluation, the cells were charged beyond the standard cutoff voltage of 3.9 V to an extended cutoff voltage of 8 V at a rate of 0.5 mA cm^{-2}, thereby intentionally imposing excessive Li plating conditions. As shown in Figure S40, the full cell employing the TREN/C-Ni-PDMS current collector exhibited a gradual and stable voltage increase, devoid of abrupt voltage decay, severe fluctuation, or clear signs of internal short circuit throughout the overcharge process. In contrast, the full cell using the Cu plate current collector exhibited early voltage instability, followed by rapid voltage collapse, indicative of dendrite-induced internal short-circuit failure.

In addition to evaluating overcharge tolerance, we further investigated mechanical abuse resistance through a nail penetration test using fully charged (100% SOC) pouch-type full cells equipped with Ni plate, C-Ni-PDMS, and TREN/C-Ni-PDMS electrodes (Figure S41). During this test, a thermocouple was strategically placed adjacent to the penetration site to monitor real-time local temperature changes. As shown in Figure S41, the three types of electrodes exhibited distinct thermal responses. The Ni plate electrode showed the highest marked thermal response following penetration. Meanwhile, the C-Ni-PDMS electrode displayed a moderately suppressed temperature rise compared to the Ni plate yet still recorded a noticeable temperature peak. In contrast, the TREN/C-Ni-PDMS electrode demonstrated superior thermal stability, exhibiting only a minimal temperature rise near the penetration site. These comparative results further support that the TREN/C-Ni-PDMS electrode can effectively mitigate thermal responses under severe mechanical abuse conditions. This enhanced thermal stability is likely attributable to its capacity for more uniform lithium deposition and improved interfacial stability in comparison to the conventional Ni plate electrode.

Collectively, these findings reinforce the notion that the TREN/C-Ni-PDMS electrode can effectively regulate lithium deposition behavior and suppress hazardous failure responses under both electrochemical and mechanical abuse conditions, thereby enhancing overall safety tolerance relative to traditional metal current collectors.

Complementary DFT calculations were conducted to clarify the interfacial behavior of the full-cell system using a practical full-cell electrolyte composed of PF_6^-, EC, DEC, and FEC. As shown in Figure S42a, PF_6^- exhibits the most negative adsorption energy among all components on the TREN-modified surface, confirming that the anion-preferential adsorption mechanism is consistently maintained. Interestingly, the adsorption energy of the FEC additive was found to be slightly lower than that of the EC solvent molecule. However, evaluating SEI formation requires considering not only adsorption affinity but also reduction kinetics. To further investigate this behavior, we calculated the LUMO energies of the FEC additive and the solvent molecules (EC and DEC). Our results show that FEC exhibits a significantly lower LUMO level (−0.84 eV) compared to EC (−0.58 eV) and DEC (−0.54 eV) (Figure S42b), indicating that FEC is preferentially reduced at the interface and thus acts as an efficient SEI former despite its lower adsorption energy. This synergistic effect, preferential anion adsorption coupled with the favorable reduction capability of FEC provides a robust theoretical basis for the enhanced stability observed in full-cell tests.

Evolution of interfacial resistance during cycling was further investigated using EIS analysis (Figure 5b). For the Li-TREN/C-Ni-PDMS anode, the Nyquist plots revealed a relatively large semicircle during the initial formation cycle, which gradually decreased after 10^{th} and 100^{th} cycles and then remained nearly unchanged up to the 500^{th} cycle. This evolution indicates the progressive formation of a more conductive and stabilized SEI, followed by the preservation of a mechanically robust interphase during long-term cycling. These observations indicate that the deposited Li forms intimate interfacial contact with the conformally Ni-coated framework, thereby maintaining electronic connectivity to the external circuit through the underlying Ni-Au conductive pathway, rather than through the insulating PDMS substrate.

To further elucidate the origin of this interfacial stability, the chemical composition on the anode surface was monitored as a function of GCD cycles (10th, 100th, and 500th cycles) using XPS analysis (Figure 5c and Figure S43). After the formation cycle, the Li-TREN/C-Ni-PDMS anode exhibited an inorganic-rich SEI predominantly composed of LiF and lithiated nitrogen species (Li_3N-like), accompanied by relatively minor organic components across all elemental spectra, consistent with the results obtained from symmetric cell measurements. Given that full-cell electrolyte does not contain nitrogen-containing interphase species formed during the $LiNO_3$-assisted pre-lithiation step, as well as to lithiated nitrogen species derived from the TREN interfacial layer. Notably, these interfacial characteristics were well preserved throughout extended GCD cycling, confirming the formation of a robust, chemically stable, and uniform interphase.

To assess practical applicability, the TREN/C-Ni-PDMS anode was further evaluated under more stringent and commercially relevant conditions. Full cells were assembled with high-loading LFP cathodes (7.83 mg cm^{-2}) and a limited lithium inventory of 2 mAh cm^{-2}, achieving a N/P ratio of ~1.7. These conditions are known to exacerbate Li dendrite formation and accelerate the depletion of active Li, thereby providing a rigorous assessment of interfacial stability. As shown in Figure 5d, the Li-TREN/C-Ni-PDMS//LFP full cell exhibited excellent cycling stability. After three pre-conditioning cycles at 0.2C, the cell delivered a high specific capacity of ~162.3 mAh g^{-1} and subsequently achieved 159.5 mAh g^{-1} at 0.5C (Figure S44). It retained 94% of this capacity after 150 cycles at 0.5C, while maintaining consistently high Coulombic efficiency throughout cycling. By contrast, the Li-C-Ni-PDMS anode without TREN monolayer initially exhibited a similar capacity but gradually degraded, ultimately failing catastrophically around the 120th cycle. This failure was accompanied by erratic Coulombic efficiency, a hallmark of dendrite-induced internal short-circuiting. These results clearly demonstrate that the TREN-assembled interface is sufficiently robust to suppress dendrite growth even under such stringent, practically relevant operating conditions.

Rate capability of the full cells was further evaluated by directly comparing Li-C-Ni-PDMS//LFP and Li-TREN/C-Ni-PDMS//LFP configurations (Figure 5e). Across the entire current range from 0.2C to 5.0C, the Li-TREN/C-Ni-PDMS full cell consistently delivered higher capacities than the unmodified Li-C-Ni-PDMS counterpart. The difference became more pronounced at elevated rates, indicating that the TREN-modified interface facilitates faster and more stable Li plating/stripping kinetics under demanding conditions. Notably, when the current rate was returned to 1.0C, the Li-TREN/C-Ni-PDMS full cell recovered ~97% of its capacity, whereas the Li-C-Ni-PDMS full cell recovered ~94%, further supporting the improved reversibility and interfacial robustness of the TREN-modified electrode. Figure 5f shows the corresponding galvanostatic discharge profiles, which exhibit the well-defined and flat LFP voltage plateaus across all tested C-rates. Consequently, the cell achieved an areal energy density of ~4.3 mWh cm^{-2} at 0.2C and retained a competitive performance of 2.7 mWh cm^{-2} even at a power density of 20.5 mW cm^{-2} (at 5.0C), underscoring its strong potential for high-power Li metal battery applications. To further evaluate the practical relevance of our system, a high-loading $LiFePO_4$ pouch full cell (17.1 mg cm^{-2}) was additionally assembled, and the corresponding electrochemical performance is provided in Figure S45. Based on an average discharge voltage of 3.31 V, the corresponding areal energy density was estimated to be approximately 8.2 mWh cm^{-2}.

3 | Conclusion

In summary, we have developed a high-performance elastomeric LMA that enables unprecedented long-term cycling stability in LMBs. This achievement stems from the self-assembled integration of a lithiophilic molecular monolayer onto a large-area elastomeric current collector featuring synergistically microscale concave patterns and nanoscale crumple architectures. The fabrication strategy involves (1) mechanical transfer of PS colloids to form ordered micro-concave features; (2) ligand-exchange LbL deposition of a conductive seed layer; (3) Ni electroplating to construct a mechanically compliant yet highly conductive elastomeric current collector; and (4) self-assembly of NH_2-functionalized TREN molecules to generate a uniformly lithiophilic surface. Importantly, the resulting lithiophilic TREN-modified C-Ni-PDMS electrodes exhibited outstanding electrochemical performance, in which cycling behavior is governed by the coupled effects of film modulus, hierarchical crumpled-concave geometry, and molecular-level lithiophilic interface engineering. In symmetric Li-TREN/C-Ni-PDMS cells, stable cycling was maintained for over 2,600 h at 1 mA cm^{-2}/1 mAh cm^{-2} and over 2,100 h at 3 mA cm^{-2}/3 mAh cm^{-2}—substantially outperforming TREN-free counterparts irrespective of structural configuration. Furthermore, full cells paired with an LFP cathode retained ~90.2% of their initial capacity after 1,000 cycles at 1C and delivered an areal energy density of 4.3 mWh cm^{-2} at 0.2C. Collectively, these results demonstrate that structurally engineered and lithiophilically modified elastomeric electrodes constitute a fundamentally robust and adaptable platform for next-generation lithium metal batteries. By synergistically integrating hierarchical mechanical compliance with molecular-level interfacial chemistry, this platform simultaneously regulates Li^+ ion flux, lowers nucleation overpotential, and stabilizes the solid-electrolyte interphase under prolonged cycling. Consequently, it enables uniform and reversible Li deposition while effectively mitigating dendrite formation, mechanical degradation, and interfacial failure even under high current densities, large areal capacities, and lean Li inventories. Beyond delivering high electrochemical performance, the intrinsic mechanical adaptability and interfacial stability of this elastomeric architecture provide critical advantages in operational safety, cycling reliability, and durability, positioning it as a broadly applicable and scalable design paradigm for advanced LMB systems.

Although the current fabrication processes—based on PS colloidal mechanical rubbing, dipping LbL assembly, and electroplating—may appear relatively complex and time-intensive, it can be readily translated into more practical and cost-effective manufacturing routes. In particular, the integration of inexpensive silica colloid–assisted mechanical rubbing, scalable LbL techniques (such as spin-coating, spray deposition, or roll-to-roll assembly), and widely adopted two-electrode electroplating systems can provide a clear and viable pathway toward large-scale production and industrial implementation.

4 | Experimental Section

Detailed experimental information is available in the part of the Supporting Information.

Author Contributions

S.C., D.N., and G.C. contributed equally to this work. S.C., D.N., S.B., Y.K., and J.C. conceived and designed the experiments. S.C., D.N., and G.C. conducted experiments and data analysis. S.L., S.P., Y.S., S.C., J.L., W.C., J.G.S., D.K., G.L., and Y.L. assisted the experimental process. S.C., D.N., S.B., Y.K., and J.C. co-wrote the manuscript. All authors analyzed the results and commented on the manuscript.

Acknowledgements

This work was supported by National Research Foundation of Korea (NRF) grant funded by the Korea government (Ministry of Science and ICT) (RS-2025-02214734; RS-2025-25413074; RS-2026-25478114, 25-ET-01, RS-2025-16063688) and generous supercomputing time from KISTI.

Conflicts of Interest

The authors declare no conflicts of interest.

Data Availability Statement

The data that support the findings of this study are available from the corresponding author upon reasonable request.

References

1. W. Xu, J. Wang, F. Ding, et al., "Lithium Metal Anodes for Rechargeable Batteries," *Energy & Environmental Science* 7 (2014): 513–537, https://doi.org/10.1039/C3EE40795K.

2. J. Liu, Z. Bao, Y. Cui, et al., "Pathways for Practical High-Energy Long-Cycling Lithium Metal Batteries," *Nature Energy* 4 (2019): 180–186, https://doi.org/10.1038/s41560-019-0338-x.

3. S. Tan, Z. Shadike, X. Cai, et al., "Review on Low-Temperature Electrolytes for Lithium-Ion and Lithium Metal Batteries," *Electrochemical Energy Reviews* 6 (2023): 35, https://doi.org/10.1007/s41918-023-00199-1.

4. L.-Q. Wu, Z. Li, Z.-Y. Fan, et al., "Unveiling the Role of Fluorination in Hexacyclic Coordinated Ether Electrolytes for High-Voltage Lithium Metal Batteries," *Journal of the American Chemical Society* 146 (2024): 5964–5976, https://doi.org/10.1021/jacs.3c11798.

5. X. Gao, Y.-N. Zhou, D. Han, et al., "Thermodynamic Understanding of Li-Dendrite Formation," *Joule* 4 (2020): 1864–1879, https://doi.org/10.1016/j.joule.2020.06.016.

6. S. Qi, J. He, J. Liu, et al., "Phosphonium Bromides Regulating Solid Electrolyte Interphase Components and Optimizing Solvation Sheath Structure for Suppressing Lithium Dendrite Growth," *Advanced Functional Materials* 31 (2021): 2009013, https://doi.org/10.1002/adfm.202009013.

7. M. Baloch, D. Shanmukaraj, O. Bondarchuk, E. Bekaert, T. Rojo, and M. Armand, "Variations on Li_3N Protective Coating Using Ex-Situ and in-situ Techniques for Li° in Sulphur Batteries," *Energy Storage Materials* 9 (2017): 141–149, https://doi.org/10.1016/j.ensm.2017.06.016.

8. H. Zhang, X. Liao, Y. Guan, et al., "Lithiophilic-lithiophobic Gradient Interfacial Layer for a Highly Stable Lithium Metal Anode," *Nature Communications* 9 (2018): 3729, https://doi.org/10.1038/s41467-018-06126-z.

9. H. Song, J. Lee, M. Sagong, et al., "Overcoming Chemical and Mechanical Instabilities in Lithium Metal Anodes with Sustainable and Eco-Friendly Artificial SEI Layer," *Advanced Materials* 36 (2024): 2407381, https://doi.org/10.1002/adma.202407381.

10. Z. Tu, S. Choudhury, M. J. Zachman, et al., "Designing Artificial Solid-Electrolyte Interphases for Single-Ion and High-Efficiency Transport in Batteries," *Joule* 1 (2017): 394–406, https://doi.org/10.1016/j.joule.2017.06.002.

11. C. Guan, W. Zhao, Y. Hu, et al., "High-Performance Flexible Solid-State Ni/Fe Battery Consisting of Metal Oxides Coated Carbon Cloth/Carbon Nanofiber Electrodes," *Advanced Energy Materials* 6 (2016): 1601034, https://doi.org/10.1002/aenm.201601034.

12. Y. Zhong, S. Zhou, Q. He, and A. Pan, "Architecture Design Principles for Stable Electrodeposition Behavior-towards Better Alkali Metal (Li/Na/K) Anodes," *Energy Storage Materials* 45 (2022): 48–73, https://doi.org/10.1016/j.ensm.2021.11.033.

13. Y. Cheng, X. Ke, Y. Chen, X. Huang, Z. Shi, and Z. Guo, "Lithiophobic-lithiophilic Composite Architecture through Co-Deposition Technology toward High-performance Lithium Metal Batteries," *Nano Energy* 63 (2019): 103854, https://doi.org/10.1016/j.nanoen.2019.103854.

14. C. Guo, Y. Guo, R. Tao, et al., "Uniform Lithiophilic Layers in 3D Current Collectors Enable Ultrastable Solid Electrolyte Interphase for High-performance Lithium Metal Batteries," *Nano Energy* 96 (2022): 107121, https://doi.org/10.1016/j.nanoen.2022.107121.

15. D. He, W. Cui, X. Liao, et al., "Electronic Localization Derived Excellent Stability of Li Metal Anode with Ultrathin Alloy," *Advanced Science* 9 (2022): 2105656, https://doi.org/10.1002/advs.202105656.

16. H. Lin, Z. Zhang, Y. Wang, X. L. Zhang, Z. Tie, and Z. Jin, "Template-Sacrificed Hot Fusion Construction and Nanoseed Modification of 3D Porous Copper Nanoscaffold Host for Stable-Cycling Lithium Metal Anodes," *Advanced Functional Materials* 31 (2021): 2102735, https://doi.org/10.1002/adfm.202102735.

17. S. H. Choi, S. J. Lee, D.-J. Yoo, et al., "Marginal Magnesium Doping for High-Performance Lithium Metal Batteries," *Advanced Energy Materials* 9 (2019): 1902278, https://doi.org/10.1002/aenm.201902278.

18. X. Wang, Z. Chen, K. Jiang, M. Chen, and S. Passerini, "3D Host Design Strategies Guiding "Bottom–Up" Lithium Deposition: A Review," *Advanced Energy Materials* 14 (2024): 2304229, https://doi.org/10.1002/aenm.202304229.

19. L.-L. Lu, J. Ge, J.-N. Yang, et al., "Free-Standing Copper Nanowire Network Current Collector for Improving Lithium Anode Performance," *Nano Letters* 16 (2016): 4431–4437, https://doi.org/10.1021/acs.nanolett.6b01581.

20. C. Zhang, R. Lyu, W. Lv, et al., "A Lightweight 3D Cu Nanowire Network with Phosphidation Gradient as Current Collector for High-Density Nucleation and Stable Deposition of Lithium," *Advanced Materials* 31 (2019): 1904991, https://doi.org/10.1002/adma.201904991.

21. S. K. Park, D. Copic, T. Z. Zhao, et al., "3D Porous Cu-Composites for Stable Li-Metal Battery Anodes," *ACS Nano* 17 (2023): 14658–14666, https://doi.org/10.1021/acsnano.3c02223.

22. C. Shan, Z. Qin, Y. Xie, et al., "Cu-CNTs Current Collector Fabricated by Deformation-driven Metallurgy for Anode-Free Li Metal Batteries," *Carbon* 204 (2023): 367–376, https://doi.org/10.1016/j.carbon.2022.12.074.

23. Z. Zhang, J. Wang, X. Yan, et al., "In-Situ Growth of Hierarchical N-Doped CNTs/Ni Foam Scaffold for Dendrite-Free Lithium Metal Anode," *Energy Storage Materials* 29 (2020): 332–340, https://doi.org/10.1016/j.ensm.2020.04.022.

24. J. Wang, M. Wang, F. Chen, et al., "In-situ Construction of Lithiophilic Interphase in Vertical Micro-channels of 3D Copper Current Collector for High Performance Lithium-metal Batteries," *Energy Storage Materials* 34 (2021): 22–27, https://doi.org/10.1016/j.ensm.2020.09.002.

25. W. Chen, S. Li, C. Wang, H. Dou, and X. Zhang, "Targeted Deposition in a Lithiophilic Silver-Modified 3D Cu Host for Lithium-Metal Anodes," *Energy & Environmental Materials* 6 (2023): 12412.

26. S.-H. Wang, Y.-X. Yin, T.-T. Zuo, et al., "Stable Li Metal Anodes via Regulating Lithium Plating/Stripping in Vertically Aligned Microchannels," *Advanced Materials* 29 (2017): 1703729, https://doi.org/10.1002/adma.201703729.

27. F. Zhao, X. Zhou, W. Deng, and Z. Liu, "Entrapping Lithium Deposition in Lithiophilic Reservoir Constructed by Vertically Aligned ZnO Nanosheets for Dendrite-Free Li Metal Anodes," *Nano Energy* 62 (2019): 55–63, https://doi.org/10.1016/j.nanoen.2019.04.087.

28. Q. Li, S. Zhu, and Y. Lu, "3D Porous Cu Current Collector/Li-Metal Composite Anode for Stable Lithium-Metal Batteries," *Advanced Functional Materials* 27 (2017): 1606422, https://doi.org/10.1002/adfm.201606422.

29. J. Luan, Q. Zhang, H. Yuan, et al., "Sn Layer Decorated Copper Mesh with Superior Lithiophilicity for Stable Lithium Metal Anode," *Chemical Engineering Journal* 395 (2020): 124922, https://doi.org/10.1016/j.cej.2020.124922.

30. L. Liu, Y.-X. Yin, J.-Y. Li, et al., "Free-Standing Hollow Carbon Fibers as High-Capacity Containers for Stable Lithium Metal Anodes," *Joule* 1 (2017): 563–575, https://doi.org/10.1016/j.joule.2017.06.004.

31. X. Ji, Z. Lin, J. Zeng, et al., "Controlling Structure of Vertically Grown Graphene Sheets on Carbon Fibers for Hosting Li and Na Metals as Rechargeable Battery Anodes," *Carbon* 158 (2020): 394–405, https://doi.org/10.1016/j.carbon.2019.11.002.

32. J. W. Shin and E. Chason, "Compressive Stress Generation in Sn Thin Films and the Role of Grain Boundary Diffusion," *Physical Review Letters* 103 (2009): 056102, https://doi.org/10.1103/PhysRevLett.103.056102.

33. C. Monroe and J. Newman, "The Impact of Elastic Deformation on Deposition Kinetics at Lithium/Polymer Interfaces," *Journal of The Electrochemical Society* 152 (2005): A396, https://doi.org/10.1149/1.1850854.

34. L. Ai, Z. Zhao, Y. Li, et al., "Stress-Relieved Hollow Porous Carbon Nanoring Structures Anchored with $ZnCo_2O_4$ Nanoparticles towards Super Stable Lithium Storage," *Chemical Engineering Journal* 499 (2024): 155903, https://doi.org/10.1016/j.cej.2024.155903.

35. L. Ye, P. Feng, X. Chen, et al., "Cu Coated Soft Fabric as Anode for Lithium Metal Batteries," *Energy Storage Materials* 26 (2020): 371–377.

36. X. Wang, W. Zeng, L. Hong, et al., "Stress-Driven Lithium Dendrite Growth Mechanism and Dendrite Mitigation by Electroplating on Soft Substrates," *Nature Energy* 3 (2018): 227–235, https://doi.org/10.1038/s41560-018-0104-5.

37. F. Zhang, N. Yi, X. Chen, et al., "A Dual-Gradient Patterned Current Collector with Built-In Stress Relief for Stable Li Metal Anodes," *Advanced Functional Materials* 36 (2025): 24447.

38. Y. Ko, H. Baek, Y. Kim, M. Yoon, and J. Cho, "Hydrophobic Nanoparticle-Based Nanocomposite Films Using in Situ Ligand Exchange Layer-by-Layer Assembly and Their Nonvolatile Memory Applications," *ACS Nano* 7 (2013): 143–153, https://doi.org/10.1021/nn3034524.

39. N. Bowden, S. Brittain, A. G. Evans, J. W. Hutchinson, and G. M. Whitesides, "Spontaneous Formation of Ordered Structures in Thin Films of Metals Supported on an Elastomeric Polymer," *Nature* 393 (1998): 146–149, https://doi.org/10.1038/30193.

40. J. Y. Chung, A. J. Nolte, and C. M. Stafford, "Surface Wrinkling: A Versatile Platform for Measuring Thin-Film Properties," *Advanced Materials* 23 (2011): 349–368, https://doi.org/10.1002/adma.201001759.

41. D.-Y. Khang, H. Jiang, Y. Huang, and J. A. Rogers, "A Stretchable Form of Single-Crystal Silicon for High-Performance Electronics on Rubber Substrates," *Science* 311 (2006): 208–212, https://doi.org/10.1126/science.1121401.

42. H. D. Espinosa and B. C. Prorok, "Size Effects on the Mechanical Behavior of Gold Thin Films," *Journal of Materials Science* 38 (2003): 4125–4128, https://doi.org/10.1023/A:1026321404286.

43. W. C. Oliver and G. M. Pharr, "Measurement of Hardness and Elastic Modulus by Instrumented Indentation: Advances in Understanding and Refinements to Methodology," *Journal of Materials Research* 19 (2004): 3–20, https://doi.org/10.1557/jmr.2004.19.1.3.

44. C. Park, T. Lee, Y. Xia, T. J. Shin, J. Myoung, and U. Jeong, "Quick, Large-Area Assembly of a Single-Crystal Monolayer of Spherical Particles by Unidirectional Rubbing," *Advanced Materials* 26 (2014): 4633–4638, https://doi.org/10.1002/adma.201305875.

45. D. Jang, Y. Kim, T. Y. Kim, K. Koh, U. Jeong, and J. Cho, "Force-assembled Triboelectric Nanogenerator with High-humidity-resistant Electricity Generation Using Hierarchical Surface Morphology," *Nano Energy* 20 (2016): 283–293, https://doi.org/10.1016/j.nanoen.2015.12.021.

46. R. Zhang, X.-R. Chen, X. Chen, et al., "Lithiophilic Sites in Doped Graphene Guide Uniform Lithium Nucleation for Dendrite-Free Lithium Metal Anodes," *Angewandte Chemie International Edition* 56 (2017): 7764–7768, https://doi.org/10.1002/anie.201702099.

47. G. Huang, J. Han, F. Zhang, et al., "Lithiophilic 3D Nanoporous Nitrogen-Doped Graphene for Dendrite-Free and Ultrahigh-Rate Lithium-Metal Anodes," *Advanced Materials* 31 (2019): 1805334, https://doi.org/10.1002/adma.201805334.

48. Y. G. Zhu, G. Leverick, L. Giordano, et al., "Nitrate-mediated Four-Electron Oxygen Reduction on Metal Oxides for Lithium-oxygen Batteries," *Joule* 6 (2022): 1887–1903, https://doi.org/10.1016/j.joule.2022.06.032.

49. H. Adenusi, G. A. Chass, S. Passerini, K. V. Tian, and G. Chen, "Lithium Batteries and the Solid Electrolyte Interphase (SEI)—Progress and Outlook," *Advanced Energy Materials* 13 (2023): 2203307, https://doi.org/10.1002/aenm.202203307.

Supporting Information

Additional supporting information can be found online in the Supporting Information section.

Supporting File: aenm71104-sup-0001-SuppMat.docx.